Probing the Interfacial Structure of Aqueous Surfactants through Helium Atom Evaporation

Xiao-Fei Gao, David J. Hood, Timothy H. Bertram, and Gilbert M. Nathanson*
Department of Chemistry, University of Wisconsin-Madison
1101 University Avenue, Madison, Wisconsin, USA 53706

Abstract

Dissolved helium atoms evaporate from liquids in super-Maxwellian speed distributions because their interactions are too weak to enforce full thermal equilibration at the surface as they are "squeezed" out of solution. The excess speeds of these He atoms reflect their last interactions with solvent and solute molecules at the surfaces of water and other liquids. We extend this observation here by monitoring He atoms evaporating from salty water solutions coated with surfactants. These surface-active molecules span neutral, anionic, and cationic amphiphiles: butanol, 3-methyl-1-butanol, pentanol, pentanoic acid, pentanoate, tetrabutylammonium, benzyltrimethylammonium, hexyltrimethylammonium, and dodecyltrimethylammonium. The helium energy distributions, recorded in vacuum using a salty water microjet, reveal a sharp distinction between neutral and ionic surfactant monolayers. Helium atoms evaporate through neutral surfactant monolayers in speed distributions that are similar to a pure hydrocarbon, reflecting the common alkyl chains of both. In contrast, He atoms appear to evaporate through ionic surfactant layers in distributions that are closer to pure salty water. We speculate that the ionic surfactants distribute themselves more loosely and deeply through the top layers of the aqueous solution than do neutral surfactants, with gaps between the surfactants that may be filled with salty water. This difference is supported by prior molecular dynamics simulations and ion scattering measurements of surfactant solutions.

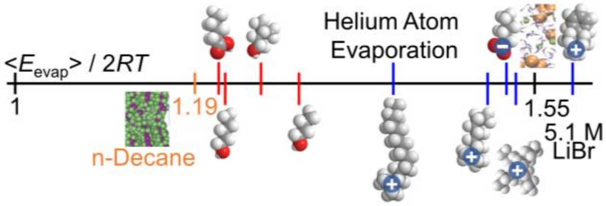

TOC Entry

1. Introduction

Surface-active (surfactant) molecules have the capacity to coat almost any water surface, including oceans, aerosol particles, and the alveoli in our lungs.[1-3] They are typically composed of a hydrophilic head group and a hydrophobic alkyl chain. These head groups span structures from neutral -OH and -COOH to charged groups such as COO^- or $-N(CH_3)_3^+$. Long-chain, nearly insoluble surfactants can efficiently impede gas transport at high packing densities,[4] but they impose much smaller barriers to evaporation and condensation when the chains are shorter and more loosely packed.[5, 6] Intriguingly, ionic head groups may even accelerate gas-liquid reactions by drawing reactive counterions such as Cl^- or Br^- to the surfaces of seawater and sea spray, where they can react with atmospheric oxidants such as N_2O_5 and O_3 to produce $ClNO_2$ or Br_2.[7-10]

The segregation of short-chain surfactants occurs by diffusion from the bulk phase to the surface region. These surfactant layers do not generally undergo distinct phase transitions like their longer chain analogues,[11-13] but continuously increase in surface concentration in a Langmuir-like way with bulk concentration. The neutral and charged head groups interact with both water molecules and dissolved ions, while the chains attract each other through dispersion forces. A powerful arsenal of techniques has been employed to investigate the segregation and packing of these surfactants, including surface tension,[14, 15] neutron reflectivity,[16-19] sum frequency generation spectroscopy,[20, 21] infrared reflection absorption spectroscopy,[22] photoelectron spectroscopy,[9, 23-26] ion scattering,[27] and molecular dynamics simulations.[25, 28-30] These methods collectively indicate that neutral surfactants segregate to the outermost layers of solution while charged surfactants tend to spread out more loosely and more deeply into solution.[16, 31-33]

We investigate here a vacuum-based technique - super Maxwellian helium atom evaporation[34-37] - that we hope will provide a new window into exploring the packing of surfactant molecules and their mixing with water and ions in the surface region. While nearly all volatile solutes evaporate from liquids in Maxwell-Boltzmann speed distributions, helium atoms evaporate on average at higher speeds and kinetic energies. In aqueous solution, these interloping He atoms slightly distort the water structure, which heals upon ejection of the He atom into the gas phase. These He atoms interact so weakly that the forces squeezing them out of solution are not dissipated in their final interactions with interfacial solvent or solute species (helium is the least polarizable atom and the least soluble in water). The He adsorption energy at the surface of water is likely to be less than RT, and He atoms approaching the surface from the bulk are immediately and “ballistically” expelled by thermal motions. In turn, the principle of detailed balance implies that a fraction of He atoms approaching from the gas phase dissolve upon collision by ballistically penetrating into solution.[38] Non-Maxwellian behavior has also been observed in the energy ejection of acetic and formic acid dimers from a water microjet[39] and non-equilibrium rotational and electronic distributions of NO evaporating from a benzyl alcohol microjet.[40] Most closely related to the studies here is the super-Maxwellian ejection of Xe atoms implanted between the tightly packed chains of self-assembled decanethiol monolayers at 135 K.[41] As the relaxing chains squeeze out the buried Xe atoms, they emerge at hyperthermal kinetic energies along the direction of the chains.

The excess kinetic energies of the evaporating He atoms depend systematically on liquid composition when compared to the reference value of 2 RT for a flux-weighted Maxwell-Boltzmann distribution at temperature T. Average helium evaporation energies are 10-20% higher than 2 RT when evaporating from hydrocarbons liquids,[34] while they are 70% higher when evaporating from highly concentrated salty water.[36] These excess kinetic energies scale roughly with the He solvation free energy, which is the integrated force acting on the He atom in the interfacial region.[36] The results reported below indicate that ionic surfactants only marginally alter the kinetic energies of He atoms evaporating from bare salty water, while neutral surfactants eject He atoms with energies closer to evaporation from pure decane, a model for the surfactant alkyl chains. These results are interpreted in terms of the differing chain density and the intermixing of water and ions between the chains.

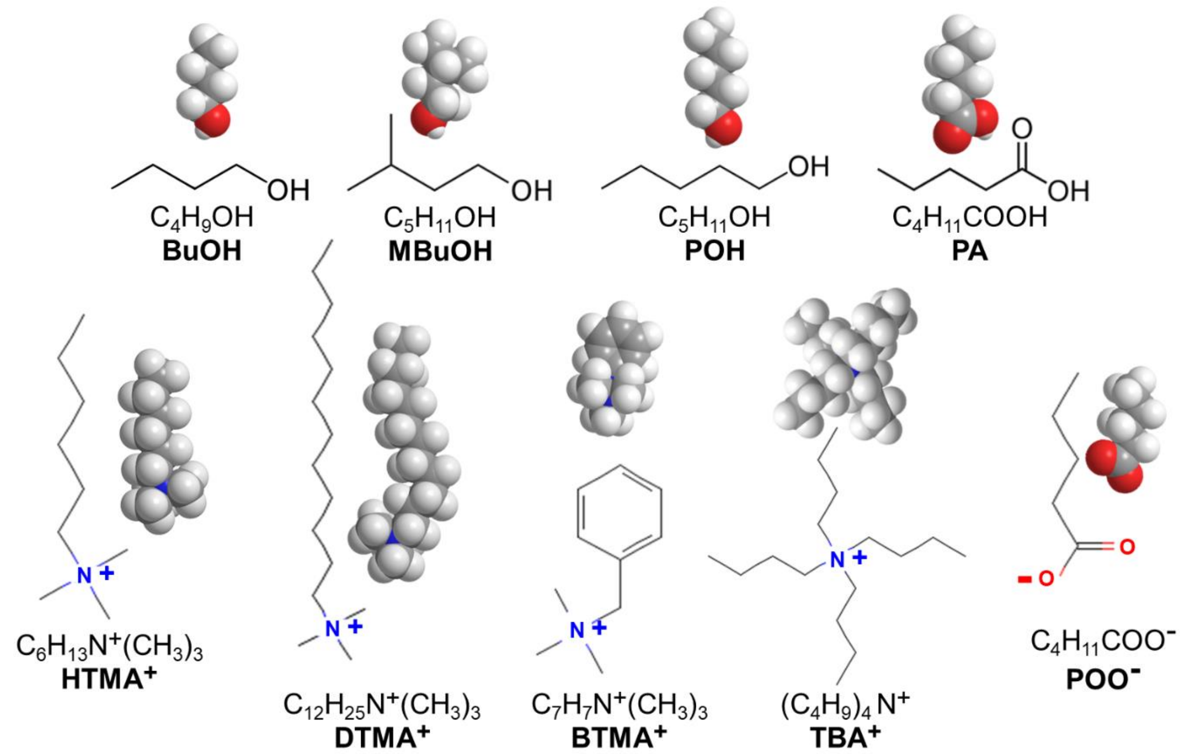

Fig. 1. Space filling models, chemical structures, and abbreviations of the surfactants used in this study.

2. Experimental Procedure

2.1 Preparing microjet solutions

The aqueous solutions consist of 5.1 M (6.0 molal) LiBr/H_2O and one of the neutral or ionic soluble surfactants shown in Fig. 1. Chemical purities are listed in Table S1 in the Supplemental Information (SI). The salty solution is made by dissolving LiBr in Millipore water, which is filtered to remove insoluble impurities. Its surface is then suctioned to remove insoluble surface-active contaminants. Each solution is prepared by dissolving one of the following surfactants: 60 mM 1-butanol, 60 mM 3-methyl-1-butanol, 60 mM 1-pentanol, 80 mM 1-pentanoic acid (conditioned to pH = 3 by adding aqueous HBr), 100 mM hexyltrimethylammonium bromide, 100 mM dodecyltrimethylammonium bromide, 50 or 150 mM tetrabutylammonium bromide, 250 mM benzyltrimethylammonium chloride (the chloride salt is purer than the bromide salt), or 74 mM lithium pentanoate (conditioned to pH = 12 by adding LiOH). The concentrations were chosen to be below the solubility limit of each surfactant, as discussed on page S10 in the SI. Microjets of pure decane and bare 5.1 M LiBr/H_2O were also prepared to compare with the surfactant solutions.

A LiBr/water subphase is used in all microjet experiments because the added LiBr salt lowers the water vapor pressure and the solution freezing point, enabling the microjet experiments to be carried out at a vapor pressure less than 1 mbar.[36] This condition is necessary to create a nearly collision free region in the vapor cloud surrounding the jet so that the energies of the evaporating He atoms are not perturbed by He-water vapor collisions (see last column of Table S2 for calculations).

2.2 He and Ar evaporation from liquid microjets in vacuum

Fig. 2 depicts the vacuum-based microjet evaporation apparatus,[42] which consists of a liquid reservoir, microjet assembly, cooled collection bottle, and differentially-pumped quadrupole mass spectrometer coupled with a spinning chopper wheel for velocity analysis. The surfactant-salty water solution in the reservoir is first degassed to expel dissolved air. The reservoir is then pressurized with He or Ar at 6 bar and vigorously shaken to saturate the solution. Two inline filters remove remaining particulates before the solution enters the nozzle. The microjet is formed from a tapered glass nozzle with a 34 µm diameter opening, which is cooled by a surrounding copper block. The jet travels at speeds of 24 m/s (255 K) or 16 m/s (235 K) and breaks up into droplets at 5 – 11 mm from the nozzle tip (see Table S2). The background pressure in the chamber housing the microjet is maintained below 1×10^{-5} mbar by liquid nitrogen-cooled panels and a 2000 L/s diffusion pump.

The speeds of the evaporating He or Ar atoms are measured by chopping the outgoing atom flux into 45 or 75 µs packets, respectively, using a rotating wheel with four 6.4 mm wide slots. Apertures in line with the mass spectrometer limit the viewing region of the microjet to 0 - 2.4 mm below the nozzle tip. The distance *L* from the chopper wheel to the electron-impact ionizer at the entrance of the mass spectrometer is 19.6 cm, and the time-of-flight (TOF) distributions for He or Ar atoms to travel this distance are recorded. Based on the microjet breakup lengths listed in Table S2, the detected He or Ar atoms evaporate from the cylindrical jet and not from droplets. The mass spectrometer views an angular average over the half of the cylinder facing it. The He angular distributions have been simulated to be slightly narrower than cosine,[46] yielding an average evaporation angle that is to be likely less than 30° with respect to the local surface normal.[34]

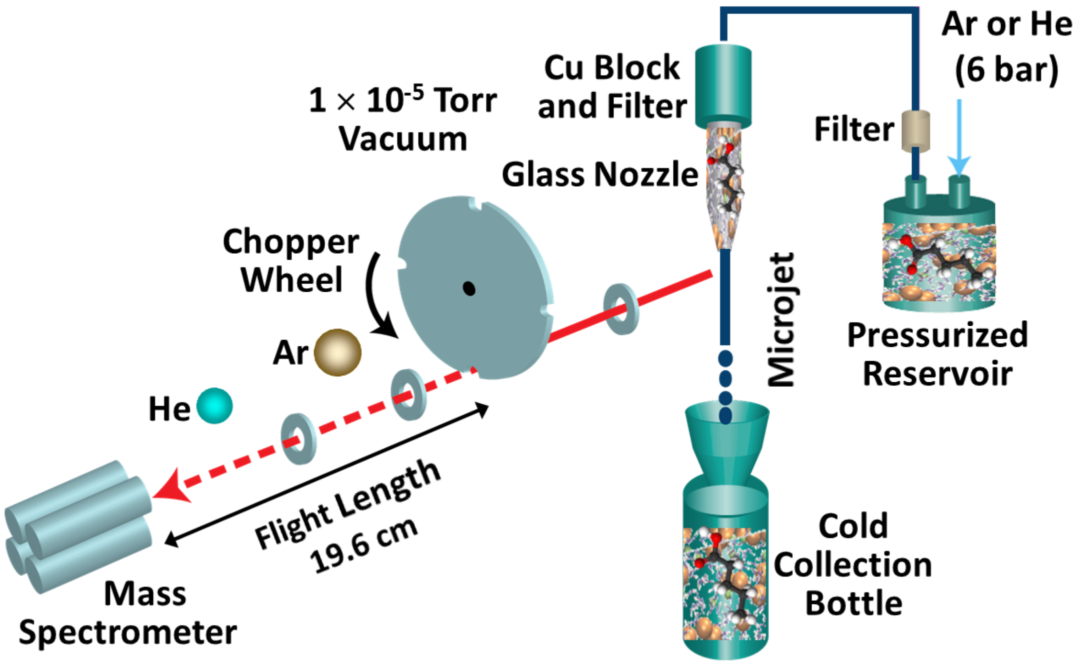

Fig. 2. Microjet apparatus for monitoring He or Ar evaporation from surfactant-coated LiBr/H_2O solutions.

The He TOF spectra yield the kinetic energy distributions of the evaporating He atoms. The observed He TOF spectra are broadened in time because of the 6.4 mm width of the chopper wheel slots and resulting 45 µs duration packets. We calculate the true TOF distribution $N(t)$ for the He spectra by convoluting a trial TOF spectrum with the wheel slot function to recover the observed TOF spectra (see ref. 36 for detailed procedures and calibration). We then use $N(t)$ to calculate the relative probability $P(E_{\text{evap}})$ of an He atom evaporating with kinetic energy $E_{\text{evap}} = ½ m_{\text{He}}(L/t)^2$. This probability is proportional to the He atom flux, $n(v)\cdot v$, where $n(v)$ is the number density of He atoms traveling at speed $v = L/t$. This flux is the number of He atoms evaporating from the jet per time and solid angle at speed v. The mass spectrometer is a flux detector with a $1/v$ ionization probability, such that the signal $N(t)$ is proportional to number density, and the variable transformation $P(E_{\text{evap}})dE_{\text{evap}} = N(t)v(t)dt$ yields the relation $P(E_{\text{evap}}) \propto N(t)t^2$. For a Maxwell-Boltzmann (MB) distribution at temperature T, the density-weighted average energy $\langle E_{\text{evap}}\rangle$ is 3/2 RT and the flux-weighted value is 2 RT (higher than 3/2 RT because of the extra factor of v in the flux).

The instrumental broadening of the TOF spectra is negligible for argon evaporation because of the heavier Ar mass and its slower speeds. These Ar atoms evaporate in a Maxwell-Boltzmann distribution, which enables the microjet solution to be fit with a temperature in the observation region. Fig. 3a and b shows Ar evaporation spectra from 5.1 M LiBr/H_2O microjets and their temperature fits of 235 and 255 K. As stated above, these temperatures were chosen in order to minimize collisions between He or Ar atoms with evaporating water molecules (Table S2 for calculations). Ar evaporation from a pure decane microjet (panel c) was also recorded in order to compare He evaporation from a hydrocarbon liquid with alkyl-chain surfactants in salty water (see ref. 34).

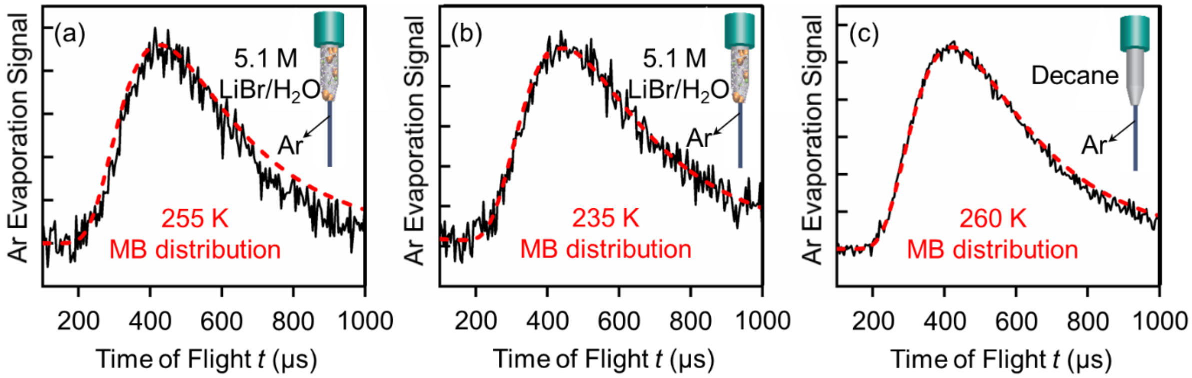

Fig. 3. Time-of-flight (TOF) spectra of argon atoms evaporating from 5.1 M LiBr/H_2O at (a) 255 K and (b) 235 K, and (c) from decane at 260 K. The solid black and red dashed lines represent the experimental spectra and Maxwell-Boltzmann (MB) distributions. Temperatures of 255, 235, and 260 K are extracted from the MB fits to within ± 10 K.

2.3 Surface Tension Measurements and Surfactant Surface Concentrations

The surface tensions γ of the surfactant solutions were measured to determine the Gibbs relative surface adsorption Γ of each surfactant. In the limit of low surfactant concentrations, the activity coefficients approach one, and the surface adsorption is given by[43]

$$\text{(1)} \qquad \Gamma = 1/RT\,(\partial\gamma/\partial \ln c_{\mathrm{bulk}})_{\mathrm{T}}$$

The value of Γ corresponds to the surfactant concentration (#/cm^2) integrated over the interfacial inhomogeneous region, which we call the "surface concentration" c_{surf}.

The surface tensions (ST) shown in Fig. 4 (left panels) are measured using the Wilhelmy platinum plate method at 290 K. The data were fit to the Szyszkowski equation[14]

$$\text{(2)} \qquad \gamma(c_{\mathrm{bulk}}) = \gamma_0 - c_{\max}\,RT\,\ln(1 + K_{\mathrm{L}}\,c_{bulk})$$

which combines eqn 1 with the Langmuir adsorption equation,

$$\text{(3)} \qquad c_{\mathrm{surf}} = c_{\max}(K_{\mathrm{L}}\,c_{\mathrm{bulk}})/(1 + K_{\mathrm{L}}\,c_{\mathrm{bulk}})$$

where K_{L} is the surface-bulk equilibrium constant and $c_{\max}$ is the maximum surface concentration. The parameters $c_{\max}$, K_{L}, and γ_0 are allowed to vary in a least-squares analysis. All fitted parameters are listed in Table S3, with a comparison to literature values in pure water in Table S4. They enable determinations of c_{surf} at 290 K shown in the right side of Fig. 4. These surface concentrations vary from 1×10^{14}/cm^2 for TBA$^+$/Br$^-$ to nearly 4×10^{14}/cm^2 for pentanol.

The surface concentrations in Fig. 4 are equilibrium values at 290 K, and may not be identical to those generated by diffusion in the fast-flowing microjet at 255 and 235 K. The center of the observation region is 1.0 mm below the nozzle tip, yielding segregation times of 42 μs at

255 K and 63 μs at 235 K. A detailed analysis of TBA^+ segregation is presented in the SI (pages S9-S14) using helium evaporation and high-energy SF_6 scattering as a function of temperature, bulk surfactant concentration, and microjet aging time. This analysis indicates that TBA^+ is nearly fully segregated to the surface of the microjet during the 42 μs aging time. Longer aging times reduce the average He evaporation energy by no more than 10%. We therefore limit our discussion to differences in the evaporation energies that are larger than this 10% uncertainty.

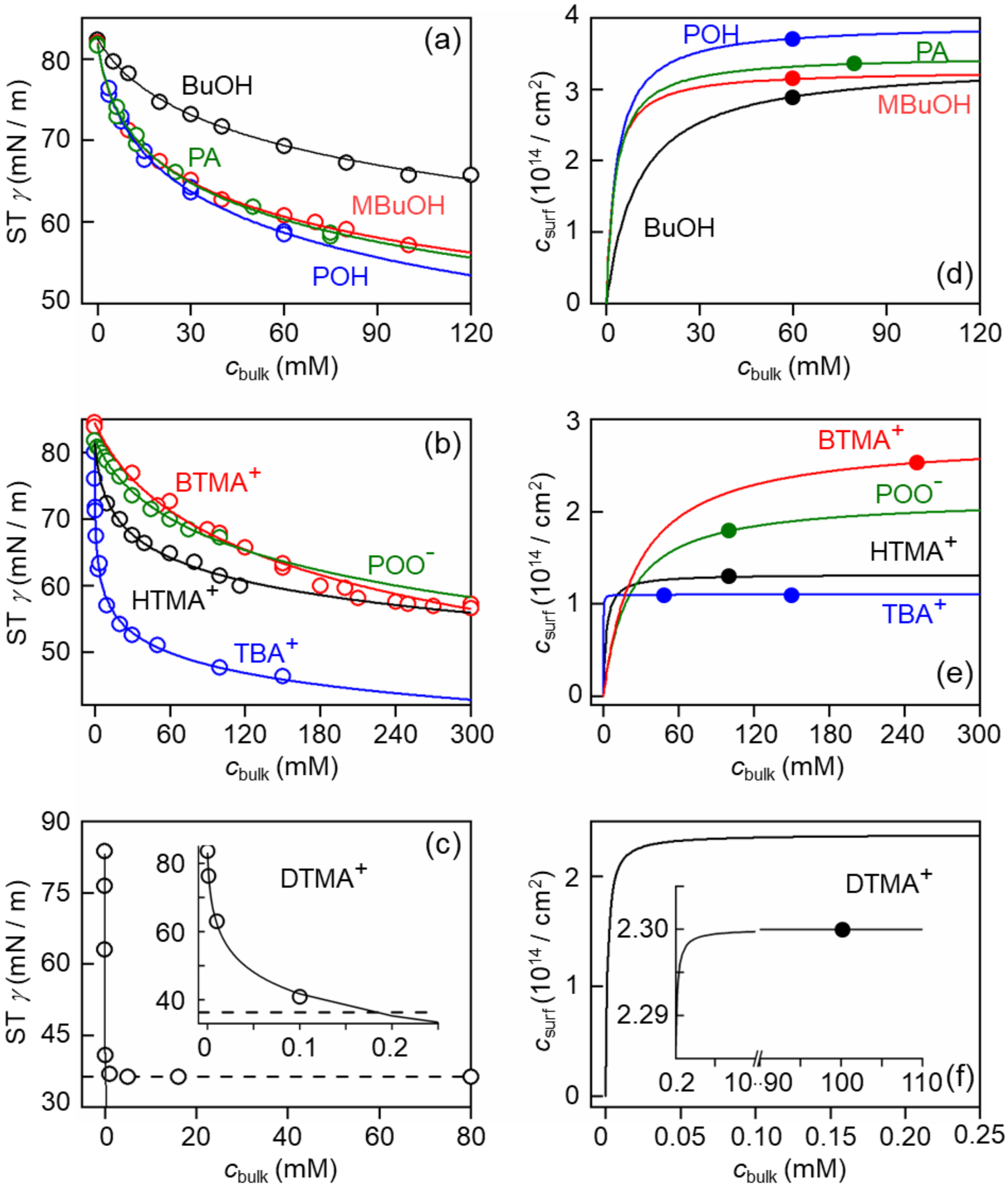

Fig. 4. Left panels (a) - (c) show the measured surface tensions (ST) γ at 290 K (circles) and the least-square fits using the Szyszkowski equation (solid lines, eqn 2). Right panels (d) - (f) show surface concentrations (c_{surf}) calculated from the Langmuir adsorption isotherm, eqn 3. The solid circles in the right panels indicate the bulk concentrations where the experiments were performed, assuming that they are equal to these equilibrium 290 K measurements. For DTMA$^+$, only four ST points with c_{bulk} smaller than the critical micelle concentration of ∽0.2 mM are fitted.[19, 44]

3. Helium Evaporation Results and Analysis

We first compare helium evaporation from bare 5.1 M LiBr/H_2O and pure liquid decane to determine the anticipated range of He kinetic energies from the surfactant-coated solutions. Fig. 5 (left panels) shows that the TOF spectra are all Super-Maxwellian, with arrival times shorter and speeds higher than a MB distribution. Panels (d) - (f) on the right display the flux-weighted He energy distributions $P(E_{evap})$ derived from the TOF spectra. They reveal that the normalized average energy, $<E_{evap}>/2RT$, is 1.19 ± 0.05 for decane at 260 K in comparison to 1.55 ± 0.07 (255 K) and 1.67 ± 0.07 (235 K) for LiBr/H_2O. Fig. S2 further shows that changes in salt concentration slightly raise $<E_{evap}>/2RT$, from 1.55 ± 0.07 for 5.1 M (6.0 molal) LiBr to 1.70 ± 0.04 for 6.7 M (8.0 molal) LiBr. Taken together, $<E_{evap}>/2RT$ generally increases with decreasing temperature and increasing salt concentration, in agreement with values recorded earlier for salty water without surfactants and for hydrocarbons.[34, 36] We note that $<E_{evap}>/2RT$ for salty water solutions is greater than 1.3[36] for pure water because ion-water binding creates an even more unfavorable helium solvation environment.[36] Both X-ray photoelectron experiments and molecular dynamics simulations indicate that Li^+ and Br^- ions populate the outermost layers of the salty solutions, such that the final collisions of the He atom may involve these ions as well as water molecules.[36,45]

Fig. 6 displays He evaporation from 5.1 M LiBr/H_2O solutions containing the neutral alcohol and carboxylic acid surfactants BuOH, MBuOH, POH, and PA (pH = 3) at 255 K. We chose these surfactants (shown in Fig. 1) because they represent different chain lengths (C_4 BuOH vs C_5 POH), chain branching (POH vs MBuOH), and head groups (POH vs PA). Panels on the left show the He TOF spectra for the neutral surfactants and panels on the right show the resulting flux-weighted He energy distributions. The normalized average energy $<E_{evap}>/2RT$ spans 1.30 for

BuOH, 1.26 for MBuOH, and 1.22 for POH and PA, with error bars of ±0.07. This key result reveals that the helium evaporation energy is just slightly greater than the value for pure decane of 1.19 and significantly lower than the bare 5.1 M LiBr value of 1.55. He atoms thus appear to evaporate through the neutral surfactant film as if they are passing through the alkyl chains of a hydrocarbon liquid.

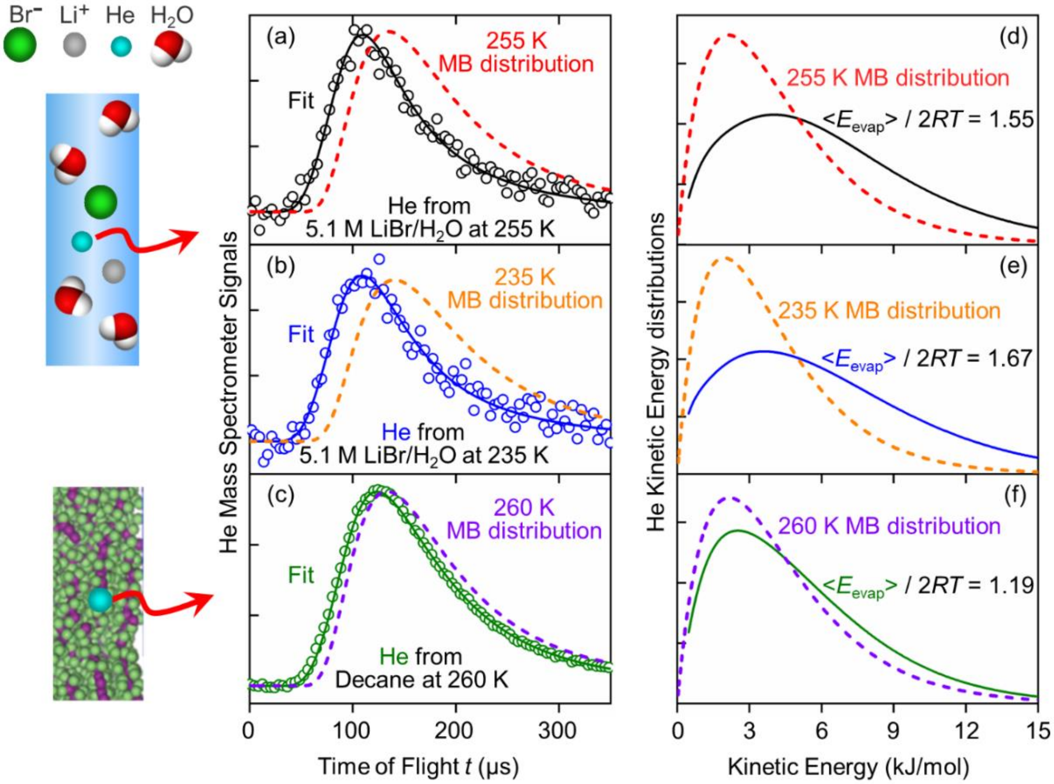

Fig. 5. Left panels show time-of-flight (TOF) spectra of He evaporation from (a) 5.1 M LiBr/H_2O at 255 K (black circles), (b) 235 K (blue circles), and (c) decane at 260 K (green circles). The solid lines are best fits to the TOF spectra. The dashed lines represent Maxwell-Boltzmann (MB) distributions of He atoms. Right panels (d) - (f) show flux-weighted kinetic energy distributions corresponding to the left panels. The curves in the right panels are area-normalized. $<E_{evap}>/2RT$ is the flux-weighted average He kinetic energy with respect to the value of 2 *RT* for an MB distribution.

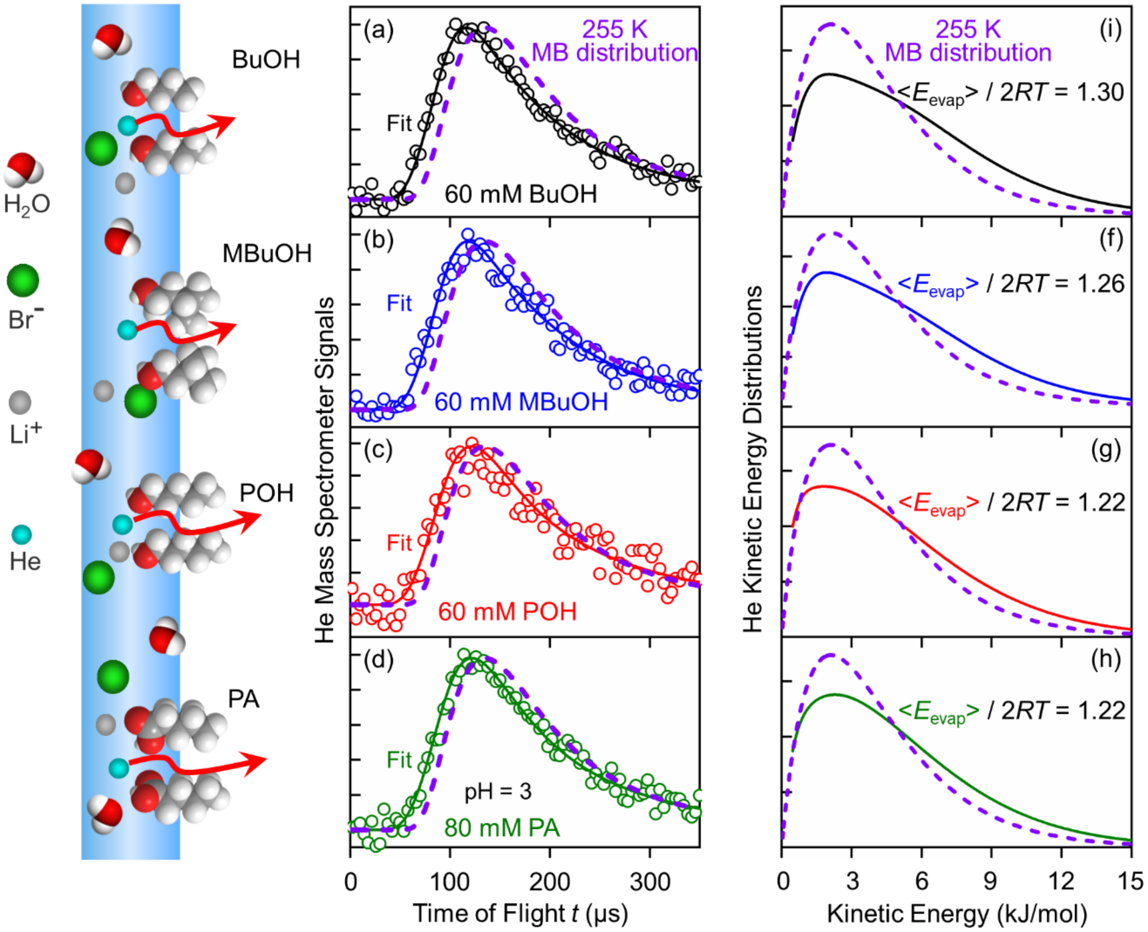

Fig. 6. Left panels show time-of-flight (TOF) spectra of He atoms evaporating from 5.1 M LiBr/H_2O solutions containing neutral surfactants: 60 mM BuOH (black circles, a), 60 mM MBuOH (blue circles, b), 60 mM POH (red circles, c), and 80 mM PA at pH = 3 (green circles, d). The solid lines are best-fits to the TOF spectra. The dashed lines represent Maxwell-Boltzmann distributions of He atoms. Right panels show flux-weighted kinetic energy distributions corresponding to the left panels (a) - (d). The curves in the right panels are area-normalized. $\langle E_{evap} \rangle / 2RT$ is the flux-weighted average He kinetic energy with respect to the value of 2 *RT* for an MB distribution.

Helium evaporation from 5.1 M LiBr/H_2O at 255 K coated with ionic surfactants (Fig. 7) behaves quite differently. The charged surfactants shown in Fig. 1 span alkylammonium cations with chains that are short (C_6, $HTMA^+$), long (C_{12}, $DTMA^+$), C_6-ring bearing ($BTMA^+$), and multiply attached (4×C_4, TBA^+). Deprotonated pentanoic acid, POO^-, is also included as an example of an anionic surfactant. The values of $<E_{evap}>/2RT$ for these surfactants are measured to be 1.40 for $DTMA^+$, 1.50 for POO^-, 1.52 for $HTMA^+$, 1.59 for $BTMA^+$, and 1.53 for TBA^+, with no apparent distinction between pentanoate (POO^-) and the cationic surfactants. These numbers constitute a second key result: the normalized He evaporation energies for ionic surfactants are closer to the value for bare 5.1 M LiBr/H_2O of 1.55, in contrast to the values for neutral surfactants, which hover closer to the 1.19 value for pure decane.

Table 1 lists the average evaporation energies $<E_{evap}>$ and average values normalized to 2 *RT* at 255 K, along with error bars. The neutral surfactant values of $<E_{evap}>/2RT$ span 1.22 to 1.30, while the ionic surfactants values span 1.40 to 1.59. Helium evaporation energies for 235 K, listed in Fig. S3, are slightly higher and show analogous trends. These trends are shown graphically in Fig. 8a, where they are seen to fall into separate groups of neutral and ionic surfactants.

Figs. 8b and c represent a search for correlations. They show how $<E_{evap}>/2RT$ varies with surfactant surface concentration c_{surf} and surface coverage θ. Panel b demonstrates a distinct trend: the normalized He evaporation $<E_{evap}>/2RT$ decreases steadily as surfactant surface concentration c_{surf} increases. The best fit line yields $<E_{evap}>/2RT = -(1.1 \pm 0.\ 1)\times 10^{-15}\ c_{surf} + (1.63 \pm 0.03)$ when $BTMA^+$ is excluded. The correlation seems robust, but the line slightly overshoots the bare 5.1 M LiBr/H_2O value by 0.08. In this graph, the separation into blocks of neutral and ionic surfactants arises from their different segregation strengths: for similar structures, neutral surfactants are generally more surface active than the ionic ones. This is particularly the case for the single methylene chain surfactants BuOH, POH, POO^-, PA, $HTMA^+$, and $DTMA^+$.

Intriguingly, panel c reveals that $<E_{evap}>/2RT$ does not correlate well with surface coverage. We calculate this coverage by setting θ equal to c_{surf}/c_{pack}, where c_{pack} is the tightest possible packing density that has been measured for each surfactant (see Table S5 for values). In this way, 1 - θ is a measure of the free surface area, assuming a single flat monolayer. We hoped that θ would reflect the likelihood that the evaporating He atom would undergo its final collision with a CH_2 or CH_3 group instead of an H_2O molecule or hydrated Li^+ and Br^- ion. We believe that this correlation fails because the tightest packing is controlled in most cases by the size of the head group (-COOH, COO^-, $-N(CH_3)_3^+$), which are larger than a CH_2 group. Panel b instead is perhaps the most appropriate measure of the chain density and free area between the chains themselves. This chain packing and the role of intermixed water and ions are the focus of the discussion below.

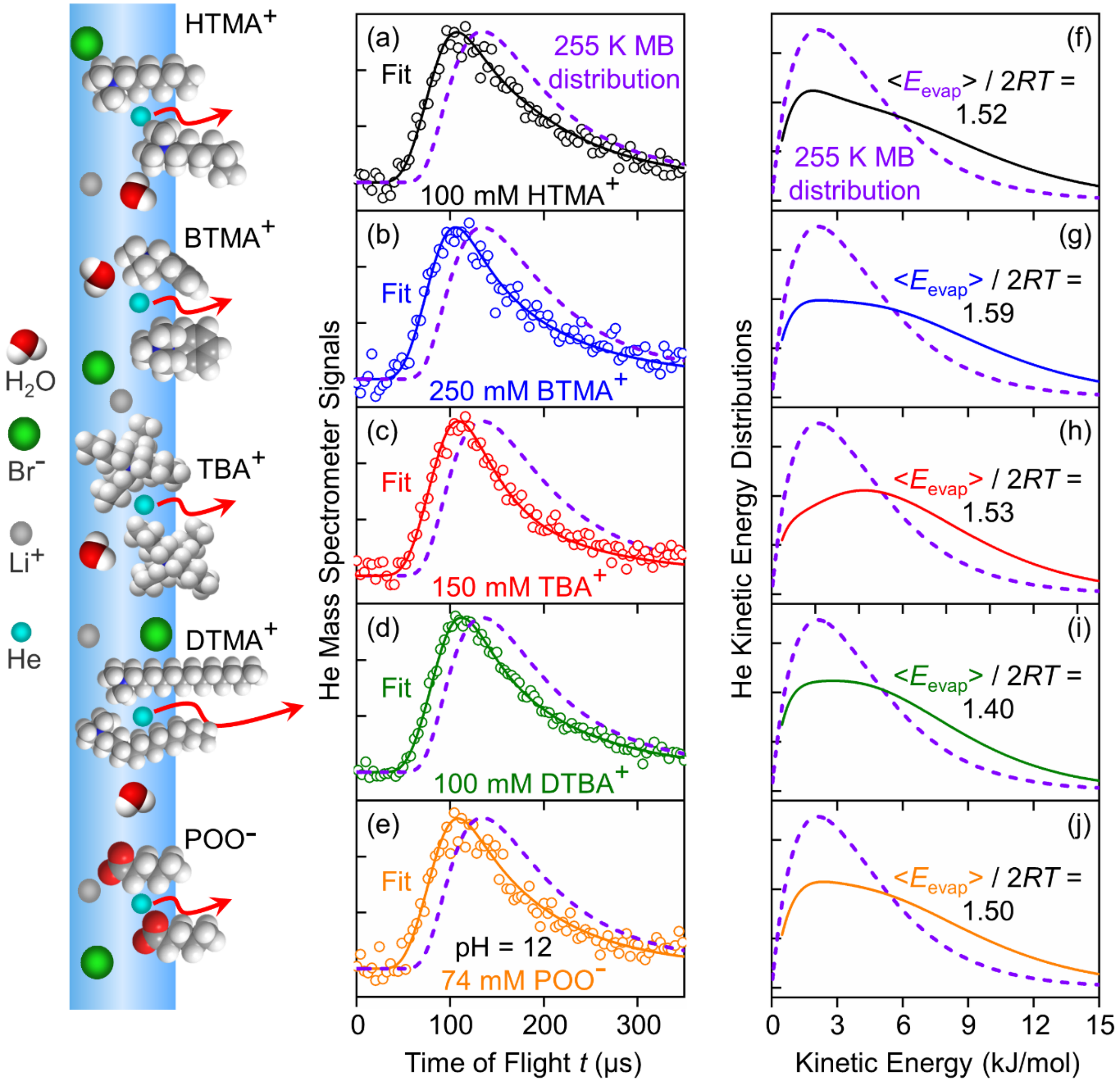

Fig. 7. Left panels show time-of-flight (TOF) spectra from 5.1 M LiBr/H_2O solutions containing the ionic surfactants 100 mM $HTMA^+$ (black circles, a), 250 mM $BTMA^+$ (blue circles, b), 150 mM TBA^+ (red circles, c), and 100 mM $DTMA^+$ (green circles, d), and 74 mM POO^- at pH = 12 (orange circles, e). The solid lines are best fits to the TOF spectra. The dashed lines represent the Maxwell-Boltzmann (MB) distributions of He atoms. Right panels show flux-weighted kinetic energy distributions corresponding to left panels (a) - (e). The curves in the right panels are area-normalized. $\langle E_{evap} \rangle / 2RT$ is the average He kinetic energy in terms of the average energy of 2 RT for a MB distribution.

Table 1 - Average Helium Evaporation Energies at 255 K

Liquids	Surfactant surface concentration (c_{surf}) [a] (1×10^{14}/ cm^2)	Average He Energy <E_{evap}> (kJ/mol) [b]	<E_{evap}>/$2RT$ [b]
5.1 M LiBr/H_2O		6.57 ± 0.30	1.55 ± 0.07
Decane		5.14 ± 0.22 (260 K)	1.19 ± 0.05 (260 K)
Neutral Surfactants in 5.1 M LiBr/H_2O			
60 mM BuOH	2.9 ± 0.3	5.51 ± 0.30	1.30 ± 0.07
60mM MBuOH	3.1 ± 0.1	5.34 ± 0.30	1.26 ± 0.07
60 mM POH	3.7 ± 0.2	5.17 ± 0.25	1.22 ± 0.06
80 mM PA	3.4 ± 0.2	5.17 ± 0.30	1.22 ± 0.07
Ionic Surfactants in 5.1 M LiBr/H_2O			
100 mM $HTMA^+$	1.3 ± 0.1	6.44 ± 0.38	1.52 ± 0.09
150 mM TBA^+	1.1 ± 0.03	6.49 ± 0.30	1.53 ± 0.07
50 mM TBA^+ [c]	1.1 ± 0.03	6.87 ± 0.30	1.62 ± 0.07
250 mM $BTMA^+$	2.5 ± 0.3	6.74 ± 0.34	1.59 ± 0.08
100 mM $DTMA^+$	2.4 ± 0.3	5.94 ± 0.25	1.40 ± 0.06
74 mM POO^-	1.7 ± 0.3	6.36 ± 0.30	1.50 ± 0.07

a. Equilibrium values at 290 K from surface tension measurements. See Table S5 for calculation of the uncertainties in the surface concentrations.

b. Three terms contribute to the uncertainties of <E_{evap}> and <E_{evap}>/$2RT$. The experimental reproducibility of <E_{evap}> and temperature uncertainty are estimated to be ± $0.01RT$ and ± 10 K. The contribution of fitting uncertainty to <E_{evap}> varies from ± 0.01 RT (decane) to ± 0.06 RT (100 mM $HTMA^+$). The listed values are flux-weighted kinetic energies, which is equal to 2 RT for a Maxwell-Boltzmann distribution.

c. 50 mM TBA^+ is not graphed in Fig. 8 but discussed in the SI on pages S10-S14.

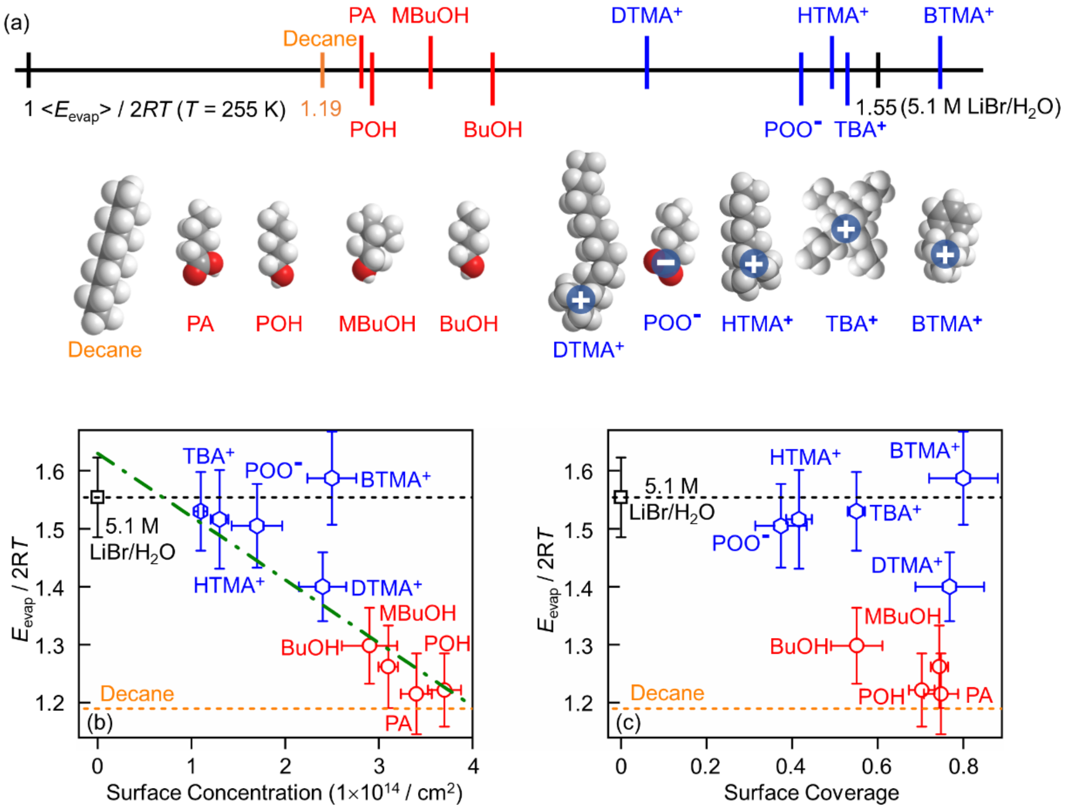

Fig. 8. (a) Line graph showing the distribution of $<E_{evap}>/2RT$ measured at 255 K in 5.1 M LiBr/H_2O, with matching surfactant molecular models below the line. (b) $<E_{evap}>/2RT$ versus surface concentration c_{surf} determined by surface tension measurements at 290 K. The best-fit line (dashed green) is a least-squares fit leaving out BTMA⁺. Note that this line slightly overshoots the value of the bare LiBr/H_2O solution. (c) $<E_{evap}>/2RT$ versus surface coverage $\theta = c_{surf}/c_{pack}$, where c_{pack} is the maximum physical packing of the surfactant. See Tables S5 for values.

4. Discussion: The Alkyl-Like and Water-Like Behavior of Neutral and Ionic Surfactants

The helium evaporation energies summarized graphically in Fig. 8a reveal two trends: He atoms evaporate through neutral surfactants with kinetic energies that mimic those of a hydrocarbon liquid like decane, while the energies of He atoms passing through ionic surfactants more closely mimic evaporation from the bare surface of salty water like LiBr/H_2O. These trends do not depend on temperature (255 vs 235 K) or LiBr salt concentration (6.0 vs 8.0 molal), as shown in the SI. The trends in Fig. 8 are perhaps best correlated with chain density, as shown in panel b.

Kann and Skinner have provided a statistical mechanical perspective in which the trends in $<E_{evap}>/2RT$ can be correlated with the potential of mean force (PMF) of the He atom in solution.[36, 46] The difference in liquid and gas end points of this potential is equal to the solvation free energy of the He atom in the liquid. This free energy is determined by the He solubility through $\Delta G° = - RT \ln K_H$, where $K_H = n(\text{He})_{liq}/n(\text{He})_{gas}$ is the Henry's Law solubility in terms of helium densities n in each phase. For He in decane and in 5.1 M LiBr/H_2O at 255 K, the values of K_H are roughly 1/5 and 1/200, yielding solvation free energies of + 3.5 and 11 kJ/mol, respectively.[36, 47] In both cases, the free energies are positive and the solubilities are less than one, driven by negative solvation entropies. The derivative of the PMF is the average force on the He atom if it moves infinitely slowly through solution and the solvent relaxes at each point. The magnitude of this force is approximate because the He atoms move with finite speeds, but the trends appear to be correct for hydrocarbon, Leannard Jones, and aqueous liquids.[34, 36, 46] In this picture, the net force on the He atom in the bulk liquid and gas is zero (flat PMF), but it is sharply positive in the interfacial region where the PMF is changing on the Angstrom scale; the larger the solvation free energy, the greater the force over similarly thick interfaces. These forces accelerate the interloping He atom through the interfacial region as the liquid structure relaxes. The excess kinetic energy arising from this acceleration for He atoms is not fully dissipated because the low polarizability and small size of He make its interactions very weak with both solvent and solutes. In contrast, almost all other atoms and molecules fully dissipate any excess kinetic energy through multiple collisions as they are momentarily trapped by the surface potential, and the solute evaporates in a Maxwell-Boltzmann speed distribution with a flux-weighted average energy of 2 RT. The excess energy of $<E_{evap}> - 2RT = 2.3$ kJ/mol (5.1 M LiBr/H_2O) and 0.82 kJ/mol (decane) reflects the inability of He atoms to fully thermally equilibrate through interfacial collisions before they exit into the gas phase. The 1.5 kJ/mol range spans RT or smaller but these differences are detectable in our experiments.

Our studies of a surfactant layer on top of water afford the opportunity to explore the intersection of hydrocarbon and salty water regions. The similar values of $<E_{evap}>/2RT$ for neutral surfactants and pure decane (and other hydrocarbons[34]) imply that the He atom loses memory of its origins in the salty water after it enters and diffuses through the hydrocarbon region, undergoing many collisions with CH_2 and CH_3 groups in a manner similar to an independent alkane liquid. The denser and longer the hydrocarbon tail, the more the He evaporation energy mimics that of decane. We note that this picture begins to break down for butanol, the shortest and least segregated of the neutral monolayers, which has an intermediate value of $<E_{evap}>/2RT = 1.30$.

Perhaps most surprising are the near-water like values of $<E_{evap}>/2RT$ for the ionic surfactants shown in Fig. 8. This similarity must arise in part from their weaker segregation to the surface. Based on a 20 Å^2 area for a CH_2 group, the 1.3×10^{14}/cm^2 density for $HTMA^+$ corresponds to filling 1/4 of the surface area when the chains are vertically aligned. The surface is therefore likely to expose some bare salty water through which the He atoms can exit. This filling is nearly complete for TBA^+, however, as shown experimentally in the SI. $BTMA^+$ is also likely to cover 3/4 or more of the surface. Yet these two surfactants enable He atoms to escape with energies nearly identical to bare $LiBr/H_2O$. One possible explanation is that the two surfactants are more compact and have higher mass densities than single methylene chains, and therefore that He atoms lose significantly less energy during their encounters with the surfactant molecules. We hope to test this hypothesis in the future by using partially fluorinated surfactants that replace CH_2 and CH_3 with CF_2 and CF_3 and increase chain stiffness.[48]

Molecular dynamics simulations of surfactants on pure water suggest an additional explanation of the high He evaporation energies in terms of the “wetness” of the monolayers. Fig. 9 reproduces MD simulations from Jedlovszky and coworkers,[30] which compares dodecanol (DOH) and dodecyltrimethylammonium (DTA^+/Cl^-) ions at 2.4×10^{14}/cm^2 surface densities (where DTACl is beyond the critical micelle concentration). While the neutral alcohol chains are nearly devoid of water molecules, the cationic film is populated throughout with water molecules as the first few methylene chains are pulled deeper in solution to better solvate the positive charge distributed across the CH_2 and CH_3 groups and N headgroup atom.[49] In this case, the final collision of some He atoms may be with water molecules rather than CH_2 or CH_3 groups. A similar water-interspersed region can be seen for TBA^+/I^- at near surface saturation in 1 M NaBr solution in simulations by Jungwirth and coworkers.[25, 28]

An additional consideration involves the very high 5.1 M LiBr concentration used in the experiments, which corresponds to a water:ion ratio of roughly 5:1. This ratio is close to the first coordination shell water:ion ratio of 4 and 6 for Li^+ and Br^- in water,[45, 50] suggesting that most water molecules are tied up in ion solvation. One intriguing possibility is that the ionic surfactants are pulled even deeper into this highly salty solution, where the distributed positive charge along the alkyl chains is solvated by Br^- ions and H_2O.[49] The deeper submersion of the surfactant ions would in turn space them farther apart laterally for the same overall surface excess. In this case, the outermost regions could be significantly more mixed with hydrated ions and water molecules. Direct evidence for this dispersal is lacking in salty water, but multilayering has been observed by neutron reflectivity in special cases.[51] We have separately observed this immersion experimentally in ion scattering studies of the ionic surfactant tetrahexylammonium bromide (THA^+/Br^-) in glycerol ($HOCH_2CH_2(OH)CH_2OH$).[52] For this strongly hydrogen-bonded liquid, the surface THA^+ and Br^- ions occupy a narrow 10 Å region that is one monolayer wide. When 0.4 M NaBr is added, the larger surface excess is spread out over 30 Å and is almost equally populated with glycerol and THA^+ and Br^- ions. Thus, the "salting out" of surfactants to the surface is manifested not by tighter packing in the outermost region but by a buildup of surfactant over several layers. The much higher LiBr concentration used here in water may create a similarly mixed region of water, Li^+ and Br^- ions, and cationic surfactants.

An intriguing attribute of such a mixed surfactant-ion-water interfacial region may be the existence of "capillary fingers" in which water is drawn up into channels between the alkyl chains. These fingers were discovered computationally for rare events in which water molecules permeate through a hexadecanol monolayer on pure water.[53] We speculatively extend this picture to hypothesize more persistent channels between the ionic surfactants depicted in Fig. 10a and b: these fingers may create a salty water network through which He atom diffuse on their way to evaporating. This mechanism is in contrast to He diffusion between the dry alkyl chains depicted in panel c. Molecular dynamics simulations may be the best immediate test of this possibility, matched by future experiments at higher temperatures near 273 K and at lower salt concentrations and even pure water. These experiments must overcome the challenges of using narrower microjets to limit He-water vapor collisions at higher vapor pressure and the consequent lower He evaporation signals.

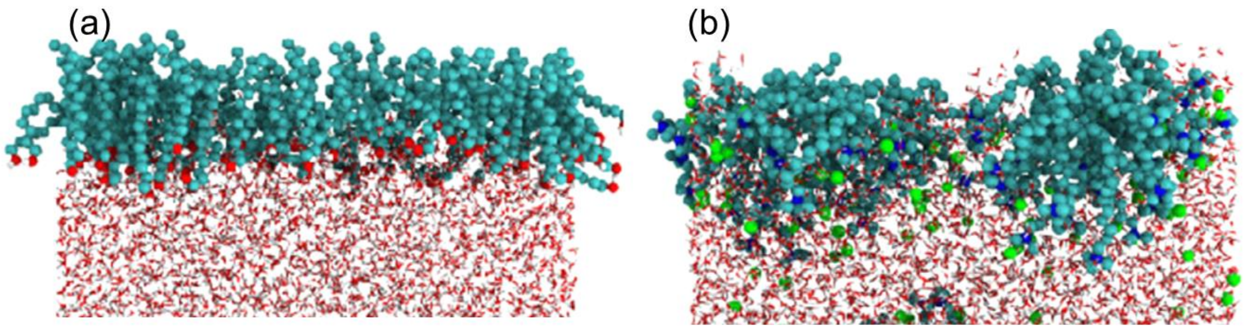

Fig. 9. Snapshots of molecular dynamics simulations of (a) water + dodecanol (DOH) and (b) water + dodecyltrimethylammonium chloride (DTAC) from Jedlovesky and coworkers.[30] The surface surfactant concentrations are each $2.4 \times 10^{14}/\text{cm}^2$. Water molecules are abundant throughout the DTAC monolayer but absent in the DOH monolayer. Adapted with permission from ref. 30. Copyright 2019 American Chemical Society.

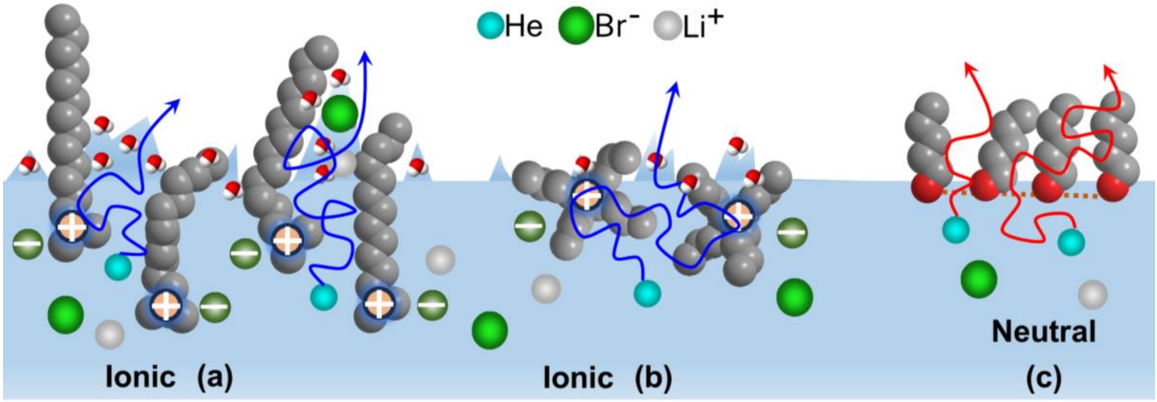

Fig. 10. Possible mechanisms for helium atom evaporation from (a, b) ionic and (c) neutral surfactant layers. Ionic surfactants may pack more loosely and be immersed more deeply than neutral surfactants. The He atoms can therefore undergo more collisions with water when evaporating through the ionic surfactant layer. In the neutral surfactant layer, the final collision of the evaporating He atoms are more often with hydrocarbon chains. The ionic surfactants are speculatively drawn with capillary water “fingers” between the chains that may provide pathways for evaporating He atoms that mimic those of bare salty water.

5. Conclusions and Outlook: Ionic Monolayers and Aerosol-Mediated Reactions

Vacuum-based microjet experiments show that helium atoms evaporate through soluble neutral and ionic surfactant layers on salty water in super-Maxwellian energy distributions. The normalized kinetic energies, $<E_{\mathrm{evap}}>/2RT$, range between 1.55 and 1.19 for bare 5.1 M LiBr/H_2O and pure decane. We find that $<E_{\mathrm{evap}}>/2RT$ lies close to the decane value for neutral surfactants (alcohols and carboxylic acids) while it resembles the bare salty water value for ionic surfactants (alkylammonium cations and carboxylate anions). These observations suggest that the alkyl chains of alcohols and carboxylic acids behave like analogous chains in a pure liquid hydrocarbon, forming a separate oily phase on top of salty water. In contrast, the alkyl groups of the ionic surfactants are nearly invisible to He atoms. This trend roughly correlates with surfactant surface concentration, as ionic surfactants tend to segregate less strongly than do neutral surfactants. This packing may even be looser because these charged species also tend to be immersed more deeply and so potentially expose more water-like patches at the surface. The water-like values of $<E_{\mathrm{evap}}>/2RT$, however, persist even for the tetrabutylammonium cation at nearly full packing. Prior molecular dynamics simulations indicate that the ionic surfactants are interspersed by water molecules.[30] We speculate that these extra water molecules might form water channels[53] that enable He atoms to move between the ionic surfactant molecules, especially for salty solutions that stabilize the charge. In this picture, the departing He atoms would then interact preferentially with water molecules and hydrated ions during their last collision within the surfactant region.

These experiments motivate a picture of water- and ion-infused surfactant layers built from charged surfactants and salty water. In one particular instance, ion-water regions that fill voids between alkyl chains would provide reactive microenvironments in the outermost regions of sea spray aerosol particles. These droplets contain high concentrations of Cl^- and Na^+ ions that are sometimes intermixed with ionic surfactants.[2, 54] In turn, this halide-rich interfacial region can enhance conversion of ambient species such as N_2O_5 into $ClNO_2$, a key photolytic source of Cl radicals in the troposphere.[10]

The helium evaporation experiments performed here imply distinct pictures of neutral and ionic surfactants at the surface of salty water. We do not yet know if these experiments teach us new features of the packing and immersion of surfactants and their intermixing with water and ions, or whether they constitute a different way of measuring surfactant properties already inferred from other methods. As in the studies of He evaporation from pure and salty water, we do know that the interpretation of these experiments will move from conjecture to deep understanding when combined with molecular dynamics simulations and the tools of statistical mechanics.[35, 36, 46] We hope that the current experiments stimulate such an incisive theoretical effort and together contribute to an even more detailed atomic-scale description of neutral and ionic surfactants at the surfaces of liquids.

Conflicts of interest

There are no conflicts to declare.

Acknowledgements

We are grateful to the U.S. National Science Foundation for supporting this research through the Center for Aerosol Impacts on Chemistry of the Environment, an NSF Center for Chemical Innovation (NSF CHE 1801971). We also thank Pál Jedlovszky for enlightening discussions about surfactants and for approval to reproduce snapshots of the molecular dynamics simulations in Fig. 9.

References

1. B. Kronberg, K. Holmberg and B. Lindman, in *Surface Chemistry of Surfactants and Polymers*, John Wiley & Sons, Ltd., 2014, ch. 1 and 12, pp. 1-47, 231-249.
2. R. E. Cochran, O. Laskina, J. V. Trueblood, A. D. Estillore, H. S. Morris, T. Jayarathne, C. M. Sultana, C. Lee, P. Lin, J. Laskin, A. Laskin, J. A. Dowling, Z. Qin, C. D. Cappa, T. H. Bertram, A. V. Tivanski, E. A. Stone, K. A. Prather and V. H. Grassian, *Chem*, 2017, **2**, 655-667.
3. F. Possmayer, Y. Y. Zuo, R. A. W. Veldhuizen and N. O. Petersen, *Chem. Rev.*, 2023, **123**, 13209-13290.
4. G. T. Barnes, *Colloid Surf. A-Physicochem. Eng. Asp.*, 1997, **126**, 149-158.
5. J. F. Davies, R. E. H. Miles, A. E. Haddrell and J. P. Reid, *Proc. Natl. Acad. Sci. U.S.A.*, 2013, **110**, 8807-8812.
6. J. R. Lawrence, S. V. Glass and G. M. Nathanson, *J. Phys. Chem. A*, 2005, **109**, 7449-7457.
7. T. H. Bertram, R. E. Cochran, V. H. Grassian and E. A. Stone, *Chem. Soc. Rev.*, 2018, **47**, 2374-2400.
8. J. R. Gord, X. Zhao, E. Liu, T. H. Bertram and G. M. Nathanson, *J. Phys. Chem. A*, 2018, **122**, 6593-6604.
9. S. Chen, L. Artiglia, F. Orlando, J. Edebeli, X. Kong, H. Yang, A. Boucly, P. Corral Arroyo, N. Prisle and M. Ammann, *ACS Earth Space Chem.*, 2021, **5**, 3008-3021.
10. D. T. Limmer, A. W. Götz, T. H. Bertram and G. M. Nathanson, *Annu. Rev. Phys. Chem.*, 2024, **75**.
11. V. M. Kaganer, H. Möhwald and P. Dutta, *Rev. Mod. Phys.*, 1999, **71**, 779.
12. D. Vollhardt and V. Fainerman, *Adv. Colloid Interface Sci.*, 2010, **154**, 1-19.
13. G. L. Gaines, *Insoluble Monolayers at Liquid-gas Interfaces*, Interscience Publishers, 1966, ch. 4.
14. C. H. Chang and E. I. Franses, *Colloid Surf. A-Physicochem. Eng. Asp.*, 1995, **100**, 1-45.
15. K. Lunkenheimer, W. Barzyk, R. Hirte and R. Rudert, *Langmuir*, 2003, **19**, 6140-6150.
16. J. R. Lu, E. A. Simister, E. M. Lee, R. K. Thomas, A. R. Rennie and J. Penfold, *Langmuir*, 1992, **8**, 1837-1844.

17. Z. X. Li, J. R. Lu, R. K. Thomas, A. R. Rennie and J. Penfold, *J. Chem. Soc., Faraday Trans.*, 1996, **92**, 565-572.
18. J. R. Lu, R. K. Thomas and J. Penfold, *Adv. Colloid Interface Sci.*, 2000, **84**, 143-304.
19. P. X. Li, R. K. Thomas and J. Penfold, *Langmuir*, 2014, **30**, 6739-6747.
20. B. A. Wellen Rudd, A. S. Vidalis and H. C. Allen, *Phys. Chem. Chem. Phys.*, 2018, **20**, 16320-16332.
21. R. A. Livingstone, Y. Nagata, M. Bonn and E. H. G. Backus, *J. Am. Chem. Soc.*, 2015, **137**, 14912-14919.
22. A. M. Deal and V. Vaida, *J. Phys. Chem. A*, 2022, **126**, 8280-8294.
23. F. Eschen, M. Heyerhoff, H. Morgner and J. Vogt, *J. Condens. Matter Phys.*, 1995, **7**, 1961-1978.
24. B. Winter, R. Weber, P. M. Schmidt, I. V. Hertel, M. Faubel, L. Vrbka and P. Jungwirth, *J. Phys. Chem. B*, 2004, **108**, 14558-14564.
25. M. J. Krisch, R. D'Auria, M. A. Brown, D. J. Tobias, C. Hemminger, M. Ammann, D. E. Starr and H. Bluhm, *J. Phys. Chem. C*, 2007, **111**, 13497-13509.
26. M. M. Walz, J. Werner, V. Ekholm, N. L. Prisle, G. Öhrwall and O. Björneholm, *Phys. Chem. Chem. Phys.*, 2016, **18**, 6648-6656.
27. G. Andersson and C. Ridings, *Chem. Rev.*, 2014, **114**, 8361-8387.
28. B. Winter, R. Weber, I. V. Hertel, M. Faubel, L. Vrbka and P. Jungwirth, *Chem. Phys. Lett.*, 2005, **410**, 222-227.
29. N. Abrankó-Rideg, G. Horvai and P. Jedlovszky, *J. Mol. Liq.*, 2015, **205**, 9-15.
30. G. Hantal, M. Sega, G. Horvai and P. Jedlovszky, *J. Phys. Chem. C*, 2019, **123**, 16660-16670.
31. E. Jarek, T. Jasiński, W. Barzyk and P. Warszyński, *Colloid Surf. A-Physicochem. Eng. Asp.*, 2010, **354**, 188-196.
32. M. Luo, N. A. Wauer, K. J. Angle, A. C. Dommer, M. Song, C. M. Nowak, R. E. Amaro and V. H. Grassian, *Chem. Sci.*, 2020, **11**, 10647-10656.
33. M. Peng and A. V. Nguyen, *Adv. Colloid Interface Sci.*, 2020, **275**, 102052.
34. D. K. Lancaster, A. M. Johnson, K. Kappes and G. M. Nathanson, *J. Phys. Chem. C*, 2015,

119, 14613-14623.

35. M. A. Williams and S. P. K. Koehler, *Chem. Phys. Lett.*, 2015, **629**, 53-57.
36. C. Hahn, Z. R. Kann, J. A. Faust, J. L. Skinner and G. M. Nathanson, *J. Chem. Phys.*, 2016, **144**.
37. G. M. Nathanson, in *Molecular Beams in Physics and Chemistry: From Otto Stern's Pioneering Exploits to Present-Day Feats*, eds. B. Friedrich and H. Schmidt-Böcking, Springer International Publishing, Cham, 2021, pp. 631-647.
38. A. M. Johnson, D. K. Lancaster, J. A. Faust, C. Hahn, A. Reznickova and G. M. Nathanson, *J. Phys. Chem. Lett.*, 2014, **5**, 3914-3918.
39. M. Faubel and T. Kisters, *Nature*, 1989, **339**, 527-529.
40. M. Ryazanov and D. J. Nesbitt, *J. Chem. Phys.*, 2023, **158**, 144703.
41. K. Gibson, N. Isa and S. Sibener, *J. Phys. Chem. A*, 2006, **110**, 1469-1477.
42. T. B. Sobyra, H. Pliszka, T. H. Bertram and G. M. Nathanson, *J. Phys. Chem. A*, 2019, **123**, 8942-8953.
43. R. Defay, I. j. R. Prigožin and A. Bellemans, *Surface Tension and Adsorption*, London : Longmans, 1966, ch. 7.
44. G. Para, A. Hamerska-Dudra, K. A. Wilk and P. Warszynski, *Colloid Surf. A-Physicochem. Eng. Asp.*, 2010, **365**, 215-221.
45. K. A. Perrine, K. M. Parry, A. C. Stern, M. H. C. Van Spyk, M. J. Makowski, J. A. Freites, B. Winter, D. J. Tobias and J. C. Hemminger, *Proc. Natl. Acad. Sci. U.S.A.*, 2017, **114**, 13363-13368.
46. Z. R. Kann and J. L. Skinner, *J. Chem. Phys.*, 2016, **144**.
47. H. L. E. Clever, *Helium and Neon - Gas Solubilities* (vol. 1), IUPAC Solubility Data Series, 1979.
48. L. M. Brusseau and V. S. Glubt, *Water Res.*, 2019, **161**, 17-26.
49. J. Heyda, M. Lund, M. Oncak, P. Slavicek and P. Jungwirth, *J. Phys. Chem. B*, 2010, **114**, 10843-10852.
50. C. D. Daub, V. Hänninen and L. Halonen, *J. Phys. Chem. B*, 2019, **123**, 729-737.
51. R. K. Thomas and J. Penfold, *Langmuir*, 2015, **31**, 7440-7456.

52. X. Zhao, G. M. Nathanson and G. G. Andersson, *J. Phys. Chem. B*, 2020, **124**, 2218-2229.
53. S. Sakaguchi and A. Morita, *J. Chem. Phys.*, 2012, **137**, 064701.
54. V. Gerard, B. Noziere, C. Baduel, L. Fine, A. A. Frossard and R. C. Cohen, Environ. Sci. Tech., 2016, **50**, 2974-2982.